An objective identification technique for potential vorticity structures associated with African Easterly Waves

Christoph Fischer[1,2,3], Andreas H. Fink[2], Elmar Schömer[3], Marc Rautenhaus[1], and Michael Riemer[4]

[1]Regional Computing Centre, Visual Data Analysis Group, Universität Hamburg, Hamburg, Germany
[2]Institute of Meteorology and Climate Research, Karlsruhe Institute of Technology, Karlsruhe, Germany
[3]Institute of Computer Science, Johannes-Gutenberg University, Mainz, Germany
[4]Institute for Atmospheric Physics, Johannes-Gutenberg University, Mainz, Germany

Correspondence: Christoph Fischer (christoph.fischer-1@uni-hamburg.de)

Abstract.

Tropical Africa and the North Atlantic Ocean are significantly influenced by African Easterly Waves (AEWs), which play a fundamental role in tropical rainfall and cyclogenesis in that region. The dynamics of AEWs can be described in a PV framework and redistribution of PV by latent heat release links PV to the important cloud and rain processes within the

5   waves. This paper introduces an innovative approach for a comprehensive identification and tracking of potential vorticity (PV) structures within AEWs. By employing AEW tracking and computing the wave phase of each point within the AEW domain using a Hilbert transform, we are able to effectively identify and collect 3-D PV structures associated with specific AEWs. To facilitate a climatological analysis, these structures are subsequently characterized by low-dimensional descriptors, including spatial information, intensity, and geometric approximations.

10   A climatological analysis reveals the seasonal evolution and the structural attributes of PV anomalies within AEWs over the study domain. PV feature locations closely align with the African Easterly Jet's latitudinal shift during the summer season. Analysis of the mean pressure level of the 3-D PV structures shows a remarkable shift during their life-cycle, indicating deep moist convection characteristics over land, and more shallow convection characteristics over the ocean. Both, composite data centered around identified AEW troughs and statistical analysis of main axes agree on an downshear tilt of the PV feature over

15   land, and a tilt to the south over the ocean. The trough-centered analysis reveals distinct differences between satellite-estimated and model-predicted rainfall. The agreement between the results of the composite analysis and the feature analysis provides confidence in our feature approach as a novel diagnostic tool. The low-dimensional representation of PV features enables the research on further statistical analyses, for example the relationship of these features with tropical cyclogenesis or as predictor for rainfall in the tropics.

1 Introduction

African Easterly Waves (AEWs) are synoptic-scale disturbances that play a crucial role in the weather and climate of tropical West Africa and the tropical Atlantic region. AEWs are quasi-periodic perturbations, typically originating over the broader Lake Chad region in central North Africa and propagating westward across West Africa, the North Atlantic Ocean and as

far as the eastern Pacific. They have drawn considerable attention due to their substantial impact on Atlantic tropical cyclone
25   (TC) genesis (e.g., Russell et al., 2017), rainfall variability over the West African monsoon region, and their role in extreme
precipitation events in this region (e.g., Fink and Reiner, 2003; Crétat et al., 2015; Engel et al., 2017). Understanding the
formation, propagation, and interaction of AEWs with the ambient (thermo-)dynamical state of the troposphere is essential for
improving the prediction of North Atlantic TCs and rainfall patterns in West Africa.

The potential vorticity (PV) framework is a fundamental fluid-dynamical concept widely utilized in extratropical meteorol-
30   ogy, including the understanding of barotropic and baroclinic instabilities, Rossby wave propagation and amplification (e.g.,
Hoskins et al., 1985), Rossby wave breaking (McIntyre and Palmer, 1983; Thorncroft et al., 1993), and the importance of latent
heat release and other diabatic processes on Rossby wave dynamics (e.g., Teubler and Riemer, 2021). Furthermore, under a
balance assumption, the wind, temperature and density fields can be derived solely from the PV field. Strong latent heat release
associated with convection or intense rainfall (Weijenborg et al., 2017; Müller et al., 2020) leads to horizontal and vertical
35   dipoles of PV, and thus rich small-scale structure. Müller et al. (2020) highlighted the correlation of strong PV anomalies and
intense precipitation and suggested that PV anomalies may serve as a proxy for evaluating intense rainfall. In the absence of
non-conservative processes, PV is materially conserved, which in combination with large PV gradients in the mid-latitudes
makes it relatively straightforward to identify and track PV features associated with Rossby waves and other large scale flow
features (e.g., Teubler and Riemer, 2021; Fischer et al., 2022; Hauser et al., 2023). In the tropics, however, much smaller PV
40   gradients and more prominent contributions of convective-scale latent heat release imply a more complex and smaller-scale
nature of the PV distribution, which is in particular true for AEWs. The PV perspective of AEWs thus faces challenges that
demand a more detailed investigation.

There exists a substantial body of research on AEWs, especially encompassing their dynamical interaction with the envi-
ronment and their relationship with TCs. For instance, Thorncroft et al. (2008) investigated the role of the African Easterly Jet
45   (AEJ) in supporting the growth of AEWs, suggesting that the AEJ alone may not be capable of supporting realistic amplitudes
of AEWs based on normal mode growth rates. From a PV perspective, Tomassini et al. (2017) highlighted the importance
of moist convection in sustaining and intensifying AEWs. They emphasized the role of diabatic processes in generating PV
anomalies, which interact with AEWs and modulate their intensity and structure. Russell et al. (2017, 2020) give insights into
the structure and sources of PV in AEWs, including the role of moist convection and its coupling with the background wave
50   environment. In terms of AEW predictability, there is strong indication that uncertainty in latent heat release can be linked to
larger forecast errors in AEW characteristics (Elless and Torn, 2018, 2019). Recently, Núñez Ocasio et al. (2020) suggested
that the type of convective organization and the location of the convection relative to the AEW trough may play a discrimi-
nating role in terms of AEW-related TC genesis in the North Atlantic Ocean. From a more theoretical perspective, Dunkerton
et al. (2009) provide a conceptual framework that links AEWs and TC genesis. In this framework, the nonlinear critical layer
55   of AEWs provides a region of recirculating air masses, in which moisture and PV may accumulate with time in relative iso-
lation from the drier and thus more hostile environment. Despite these potential applications in understanding AEW growth,
predictability and their role in TC genesis, the application of a PV-centric view, especially in three dimensions, in studying
AEWs has been relatively limited.

In this study, we address this gap by providing a comprehensive tool for the PV-centric analysis of AEWs. Specifically, we
address the following objectives:

- We propose a novel identification and tracking technique for 3-D PV features associated with AEWs. It facilitates the
  quantification of feature properties in case studies and climatological analyses. Objective identification techniques for
  atmospheric features have proven beneficial in both atmospheric research for statistical analyses and verification tasks,
  and in operational meteorology (e.g. Hengstebeck et al., 2011; Josipovic et al., 2022). By describing features by a low-
  dimensional vector, statistical analyses including feature climatologies (Limbach et al., 2012), ensemble forecast analysis
  (Rautenhaus et al., 2015a), and statistical postprocessing (Rasp and Lerch, 2018) can be performed.

- We perform a climatological analysis of these identified PV features to explore the properties of these features over their
  life-cycle. Furthermore, it provides confidence in the previously introduced method by comparing the identified features
  to climatological PV composites.

Multiple approaches exist for objectively identifying AEWs. Early approaches by Burpee (1972); Reed et al. (1988); Died-
hiou et al. (1999) focus on the identification of mean tracks rather than individual wave anomalies. In order to be able to
compute climatologies and to perform statistical analyses of the data, an objective identification is absolutely vital. Fink and
Reiner (2003) summarize the strength and weaknesses of automatic and manual approaches. Thorncroft and Hodges (2001)
were the first ones to exploit the usefulness of the vorticity measure to objectively track individual AEWs in the tropics. Other
approaches include the identification using Hovmöller diagrams (Bain et al., 2014). Berry et al. (2007) and Belanger et al.
(2016) most recently used the advection of curvature vorticity (CV) as primary measure of AEW activity and to identify wave
tracks. This measure proved to be very robust after applying downscaling and smoothing operators.

To reach the aforementioned goals of this work, we employ a technique similar to the one by Belanger et al. (2016) to
get a robust position of AEWs on 700 hPa, this is outlined in Sect. 2.2 and 2.3. Then, in Sect. 2.4, we compute the wave
phase at every point in the domain by performing a Hilbert transform, which is required to narrow down the regions around
AEWs where high PV associated with these AEWs is expected (Fink and Reiner, 2003). Then finally, in Sect. 2.5, we will
identify and extract the PV structures. The identified 3-D features are assigned geometric descriptions as low-dimensional
representation, including a best-fitting ellipsoid. Section 3 shows results of a climatological analysis of this features, shedding
light on the distinct characteristics of the waves. Additionally, the approach is being verified through comparison with PV
composites. A trough-centered analysis highlights differences between satellite-estimated and model-predicted rainfall. The
paper is concluded in Sect. 4, where we will discuss the implications of our findings, their relevance to previous research, and
potential avenues for further investigation.

2 Strategy

2.1 Data

For the identification of AEWs, the corresponding PV features and for the analyses in this study, we use pressure level data
from the global ERA-5 reanalysis (Hersbach et al., 2020) for the months June to October matching the West African Monsoon
season (Fink et al., 2017), on a regular grid with a grid-point spacing of $0.5°$ in both latitude and longitude, with a temporal
resolution of 6 hours. This time scale is sufficient since AEW characteristics do not vary on hourly timescales. To identify the
wave trough of AEWs, we use the zonal (u) and meridional (v) wind components at 700 hPa, where the African Easterly Jet
has its maximum speed (Fink et al., 2017). The study domain covers the region of AEW activity over tropical West Africa
and parts of the North Atlantic Ocean, specifically from 75°W to 45°E and 0°N to 40°N. The PV analysis is conducted on
16 pressure levels between 200 and 900 hPa, with intervals of 50 hPa. We exclude the pressure levels beneath 900 hPa where
surface-induced effects come into play. For rainfall analyses, the satellite-gauge based GPM IMERG V06B data set (Huffman
et al., 2015) and the twice-daily ERA-5 short-range forecasts will be used to quantify rainfall in relation to AEWs and PV
occurrence.

2.2 Identification of AEW wave troughs

To robustly identify PV features within AEWs, we build on the method by Belanger et al. (2016) to firstly identify AEW
troughs on 700 hPa. Their method is an improvement over previous work (e.g., Thorncroft and Hodges, 2001) by applying
CV instead of other vorticity measures and by ensuring that waves are westward propagating, more closely aligning with
the characteristics of AEWs. While our identification and filtering are strongly motivated by Belanger et al. (2016), we have
improved the tracking of the waves to achieve more robust and consistent tracks. Additionally, we introduce a data structure to
facilitate the analysis of the tracks, including the identification of split and merge events, computation of average wave speeds,
and other parameters.

Following the approach outlined in Belanger et al. (2016), the identification of AEW troughs is based on CV anomalies. A
climatology of CV is computed for each month and each time of day to take into account both seasonal and diurnal effects.
Then, the CV itself is bandpass-filtered to only retain frequencies that are linked to AEW disturbances. We use a filter to
keep frequencies between 2–8 days, following Russell et al. (2020). To identify wave troughs at a given point in time, we
compute the anomalies of the CV (CVA) by subtracting this bandpass-filtered CV from the climatology. In the idealized case
of westward-propagating waves, positive CVAs are linked to cyclonic rotation present in the wave trough, while negative
CVAs are present in the ridge regions. Fig. 1a shows an example of CV anomalies. The bandpass-filtered wind leads to distinct
alternating positive and negative poles of CVA. Following Belanger et al. (2016), the data is smoothed twice using a 9-point
local smoother, which retains only the synoptic-scale easterly wave structure, and three masks are applied:

- the zonal wind must be $u < +2.5 \text{ms}^{-1}$,

- the CVA must be over the 66-th percentile of the entire reanalysis,

120   – and the advection of CVAs must be equal to 0.

This set of masks locates the wave troughs. However, some wave ridges (local minima in CVA) might also exceed the 66-th percentile of the CVA climatology. Thus, the second derivative of the CVA is consulted to extract only local maxima in the data set. In Fig. 1a, the grey lines indicate zeros of CVA advection, which collocate with troughs and ridges. The red lines are then the result of applying the other masks and filters to the data set. This results in the identified wave troughs.

2.3   Tracking of AEW wave troughs

To form tracks from the identified individual wave troughs, we employ an overlap approach as followed: At each time step t, we compare the location of a wave trough with all identified wave troughs at the two subsequent time steps $t + \Delta t$ and $t + 2\Delta t$ with $\Delta t = 6\,\mathrm{h}$. With this approach, wave tracks can persist even when the trough is not detected at $t + \Delta t$. This happens, when one of the above mentioned identification masks is not fulfilled for this time step, but for the ones before and after. Consequently,

130   maintaining longer continuous wave tracks, rather than multiple short tracks, enhances the quality of the tracking results. Given the shape of the wave trough, as depicted in Fig. 1b, we generate a polygon defined by the area where we would expect the AEW to be in the next time step. This area is defined by the expected propagation speed, which we set to the range between $u_{max} = -15\,\mathrm{ms^{-1}}$ to $u_{min} = +2\,\mathrm{ms^{-1}}$. While AEWs typically propagate with a speed between $5\,\mathrm{ms^{-1}}$ and $10\,\mathrm{ms^{-1}}$ (Gu et al., 2004), we use a broader range to account for sampling artifacts due to the resolution and to keep more tracks in general.

135   Nonetheless, based on the expected wavelength of AEWs (e.g., Fink et al., 2017), this range still ensures we do not mix up different waves into the same track. Given a time granularity Δt, the bounds of expected traveled distance d_{min} and d_{max} can be computed by multiplying u_{min} and u_{max} with the elapsed time. Consequently, when comparing wave troughs with a time difference of 12 hours, the resulting polygon covers twice the area compared to a 6-hour difference.

Using the identified connections, a connection graph $G = (W, E)$ is formed, similar to the one introduced by Limbach

140   et al. (2012). Here, W represents the set of all wave troughs and serves as the nodes in the graph, while E denotes the edges connecting elements of W. A pair of wave troughs $w_1, w_2 \in W$ forms an edge $(w_1, w_2) \in E$ if they represent the same entity, thus, fulfilling the overlap strategy outlined above. This graph provides a concise representation of the union of all wave troughs and their evolution over time. For instance, if there exist two wave troughs w_1, w_2 following wave trough w, such that $(w, w_1) \in E$ and $(w, w_2) \in E$, the wave trough splits in two, indicating a split event. The connection graph is being simplified

145   by removing transitive edges that are primarily introduced through the comparison of wave troughs from non-consecutive time steps. Thus, if all $\{(w_1, w_2), (w_2, w_3), (w_1, w_3)\} \subseteq E$, then (w_1, w_3) is eliminated from E.

After the connection graph has been simplified, tracks are extracted from the graph. Each track T^i itself is a graph $T^i = (W^i, E^i)$, based on a subset of wave troughs $W^i \subseteq W$ and connections $E^i \subseteq E$. The tracks T^i are disjoint subsets of the overall connection graph G. The extraction of tracks poses challenges: Features as they evolve and interact with the environment might

150   split and merge with other features. Therefore, different sets of tracks can be justified as a solution to this problem. Here, we adhere to the rule to generate tracks with the longest possible life span. This makes it easier to investigate the life cycle of these waves. To achieve that, the graph G is scanned and each node is assigned a time until dissipation. Then, tracks are formed
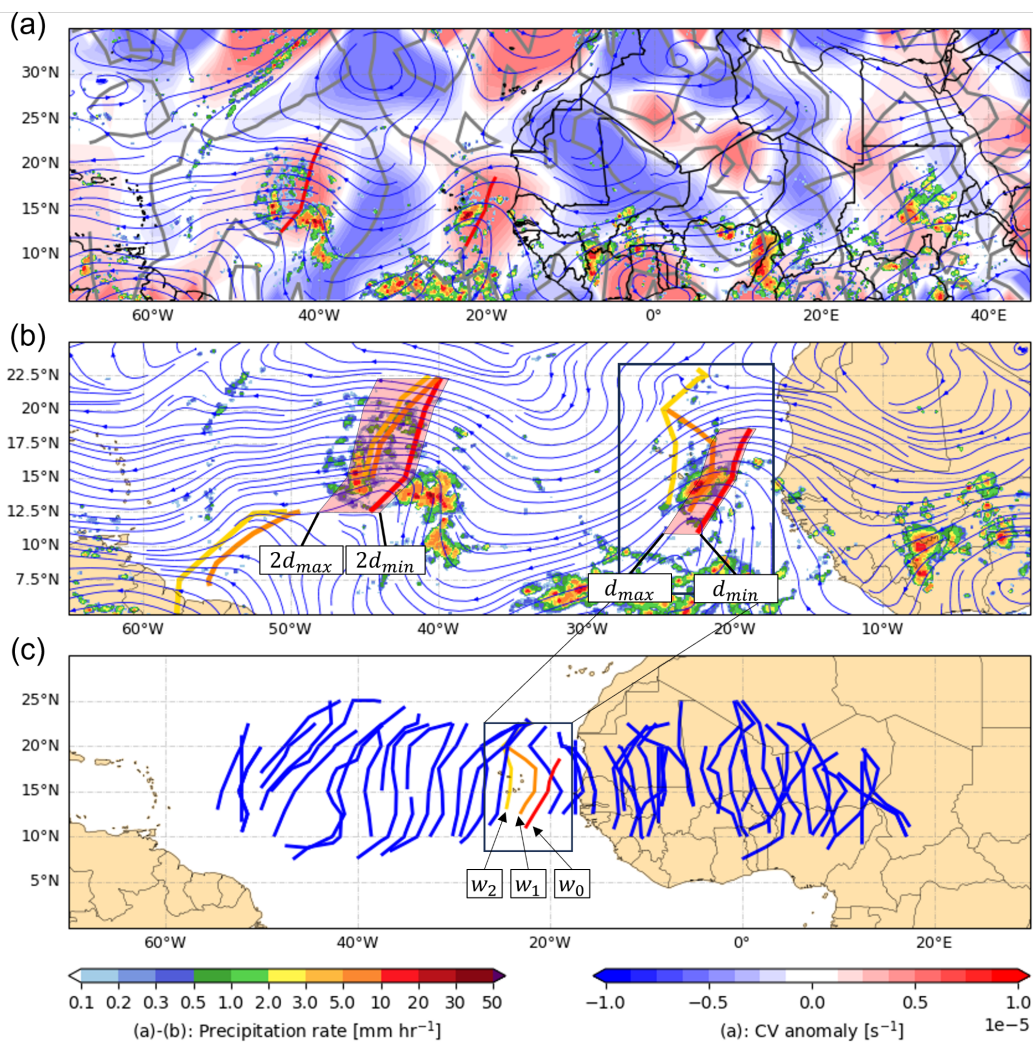
Figure 1. Illustration of the identification and tracking process for AEWs using a polygonal search approach. (a) shows the 700 hPa streamlines (blue lines) of the bandpass-filtered wind, along with CV anomalies and the precipitation rate according to the GPM IMERG data set at 13 September 2022, 00 UTC. Grey lines indicate the zeros of CVA advection, and the red lines show the the extracted wave troughs based on the filters introduced in Sect. 2.2. In (b), two identified wave troughs are shown at 00 UTC (red, as in (a)), 06 UTC (orange), and 12 UTC (yellow). Red boxes sketch the polygonal search areas computed for both wave troughs, initiated at 00 UTC. The left wave trough is compared with the +12 h wave trough, while the right wave trough is compared with the +6 h wave trough. In panel (c), an entire AEW track is depicted, demonstrating the continuity of the tracking process. The three wave troughs from (b) are highlighted.

starting from the nodes with the longest time until dissipation. In case of split events, only the track with the longest time until dissipation is continued, the other sub-track forms a different track. Subsequently, the extracted tracks T^i can be individually

155 analyzed and filtered. For each track, we compute its current speed as the average speed over a 2-day window centered around any given time step. We discard parts of tracks with an average speed of less than 3 ms^{-1} at any given point in time. This removes stationary features based on orographic effects. Furthermore following Belanger et al. (2016), we also remove tracks with a lifetime of less than 2 days from the track set.

Figure 1c shows the full life-cycle of one tracked AEW from (b). Each AEW trough represents a node in the graph. The

160 troughs of the depicted track are linked using edges: The w_0 manifestation of the wave is connected to w_1, thus $(w_0, w_1) \in E$. w_1 itself is connected downstream to the next trough w_2, and so on. When the track splits, both ways can be continued in this way. We refer to Limbach et al. (2012) for a detailed introduction on this type of data structure.

The output of the tracking algorithm consists of a list of AEW troughs with unique identifiers and their descriptions, and a list of tracks where each track is defined by a list of edges defining that track. The location of the AEW is defined as a

165 line string, thus a list of latitude-longitude points. We computed AEW trough data for the entire ERA-5 reanalysis from 1940 to 2022 and is available as stated in the data availability section. Also, a near real-time implementation displaying identified waves from the ECMWF, GFS and ICON deterministic forecasts is available[1].

2.4 Phase Computation

Although an AEW trough defines the line of maximum CV, its location does not necessarily coincide with the expected region

170 of maximum PV anomalies due to complex interactions of waves with diabatic PV generated from convection. As highlighted by Shapiro (1978) and Tomassini et al. (2017), especially over Africa, convection is mainly triggered ahead, i.e. west, of the AEW trough due to the atmospheric conditions being most conductive (Reed et al., 1977; Fink and Reiner, 2003). Over the ocean, convection is more centered on or slightly to the east of the wave trough (Riehl, 1954). However, the entire region of positive CV around the identified wave trough can be prone to convection. To quantify these areas, it is desired to assign every

175 point in the domain its current phase. For example, looking at the meridional wind component v in the background flow, the trough area can be assigned a phase between $-\pi$ to 0, and the ridge a phase between 0 and π. However, it is not straightforward to extract the phase information from a real-valued field, since all frequencies in the bandpass-filtered range of 2–8 days can contribute to it.

Zimin et al. (2003) faced a similar problem and utilized digital signal processing methods to extract amplitude and phase

180 information of Rossby wave packets. Using the so-called Hilbert transform (see a practical introduction in Purves, 2014), a complex (consisting of a real and imaginary) field can be computed from a real-valued field, which provides additional information such as amplitude and phase. This method involves performing a Fourier transform on the signal and then applying a back-transform only to the positive part of the frequency spectrum. This approach is suitable for wave patterns that encompass a range of wavenumbers, like tropical waves do. Following Zimin et al. (2003), we look at the meridional wind component v

---

[1]www.kit-weather.de/aew_deterministic_maps.php (last accessed at 09 Oct 2023)

along a latitude circle and perform a 2-D Discrete Fourier Transform over both the wavenumber and time domains:

$$V_{f,k} = \sum_{t=0}^{T-1} \sum_{n=0}^{N-1} v(t,n) e^{-2\pi j (f \frac{t}{T} + k \frac{n}{N})}, \tag{1}$$

where t denotes the time step in the data set consisting of T time steps, and n the longitude index out of N indices, while f and k denote the frequency and wavenumber coefficients of the transformed signal. Following Reed et al. (1977) and Russell et al. (2020), we choose a wavelength of 2000–6500 km and a wave frequency of 2–8 days to identify perturbances that can be assigned to AEWs. Therefore, the back transformation is only applied for the subset the positive wavenumbers $k_{min} \leq k \leq k_{max}$ and positive frequencies $f_{min} \leq f \leq f_{max}$ corresponding to the chosen wavelength and frequency criteria:

$$v_H(t,n) = \frac{2}{TN} \sum_{f=f_{min}}^{f_{max}} \sum_{k=k_{min}}^{k_{max}} V_{f,k} e^{2\pi j (f \frac{t}{T} + l \frac{n}{N})}. \tag{2}$$

This process can be described as a bandpass-filter that generates complex wave information. The real part of the restored signal represents the bandpass-filtered data. Additionally, the imaginary part allows for the computation of the phase at any point in the domain using the equation:

$$\theta(v_H) = arctan(\frac{Im[v_H]}{Re[v_H]}). \tag{3}$$

Figure 2 provides an illustration of a wind field at 700 hPa, along with the identified wave troughs highlighted in red. To remove phase signals in the trough area $(-\pi \ldots 0)$ that not near any AEW trough at all (e.g., vorticity anomalies from other tropical and extratropical waves), we restrict the validity of the phase to a radius of 1000 km around the trough line, depicted by the red contour in Fig. 2. Since the transform is performed for wavelength greater than 2000 km, this ensures we consider a substantial area that does not interfere with signals of other waves. The shading represents the phase of the wave at each point in the domain periodically from $-\pi$ to π. The wave troughs clearly align with a phase of $-\frac{\pi}{2}$ (white areas). The hatched area in Fig. 2 represents the designated search area for PV, called "trough area" from hereon, which is determined by the areas in the trough phase and near a wavetrough (within the red radius).

This highlights that the Hilbert transform produces correct results with regard to the expected wave signal. In regions that are not favorable for AEW activity, the Hilbert transform becomes more unreliable and produces artifacts. This is expected due to the fact that atmospheric waves in these areas have other frequencies and wavelengths. In addition, the green iso-contours in Fig. 2 indicate the vertically averaged PV in the lower and mid troposphere, highlighting the regions of high PV. Notably, these high PV areas align well with the phase and proximity to the wave troughs.

2.5 Identification of PV features

These previously identified trough areas in Sect. 2.4 delineate the search area for PV. Analyses of the PV field (e.g., Fig. 3), supported by 3-D analyses using Met.3D (Rautenhaus et al., 2015b), have indicated that a threshold of 0.7 PVU retains the strong signal associated with the waves while effectively separating the clusters. Therefore, we identify all grid points within trough areas that have a PV value exceeding 0.7 PVU. Figure 3a displays a raw 3-D PV field in the tropics, visualized using
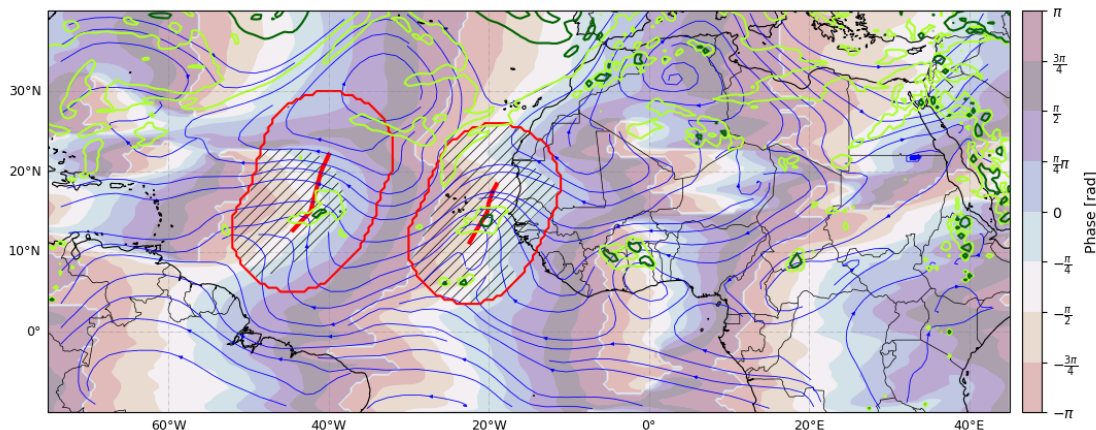
Figure 2. Visualization of the computed wave phase using a Hilbert transform (shading), and the identified wave troughs with a 1000 km radius in red at 13 September 2022, 00 UTC. The hatched region represents the intersection of the expected phase and the vicinity area of the wave trough, delineating the search area for high PV. High PV regions are indicated by the green iso-contours (light green 0.4 PVU, dark green 0.8 PVU), which are based on the averaged PV values between 900 and 300 hPa.

215   the 0.7 PVU iso-contour. The noisy PV field highlights the need for a procedure to extract PV that is linked to AEWs. In Fig. 3b, the PV areas over this threshold areas have been confined based on the trough areas defined in Sect. 2.4, and displayed as yellow volumetric objects. Additionally, a so-called morphological opening filter got applied to these objects to refine the features. This filter, as introduced by Najman and Talbot (2013) and previously applied to extratropical PV features by Fischer et al. (2022), removes small outliers while preserving the shape of a structure. Based on the proximity to the 2-D wave trough

220   lines, each PV feature can be linked to such a wave trough. Furthermore, the tracks of the 3-D PV anomalies can be inferred from the tracks of the 2-D wave troughs, as introduced in Sect. 2.3. A set of feature descriptions is computed for each PV feature, consisting of bounding box, maximum and average PV value, volume, and as outlined next, a set of image moments and a geometric representation.

2.6 Ellipsoid Computation

225   To facilitate statistical analyses of the identified features, it is desirable to represent them using a set of intuitive and well-suited parameters. Previous studies have revealed that the structure and orientation of PV features in AEWs depend on different factors, for example their location and the dynamic constraints of the environment (Tomassini et al., 2017; Russell et al., 2020). Ellipsoids are deformed spheres and can be defined by their center and their three main axes. This simple representation encapsulates information about the shape's position, size, orientation, and elongation, while being defined by only four vectors.

230   It has been termed as the "most economical representation" for meteorological observations by Smith and Woolf (1976), is also employed in various other scientific fields, including robotics and metrology.
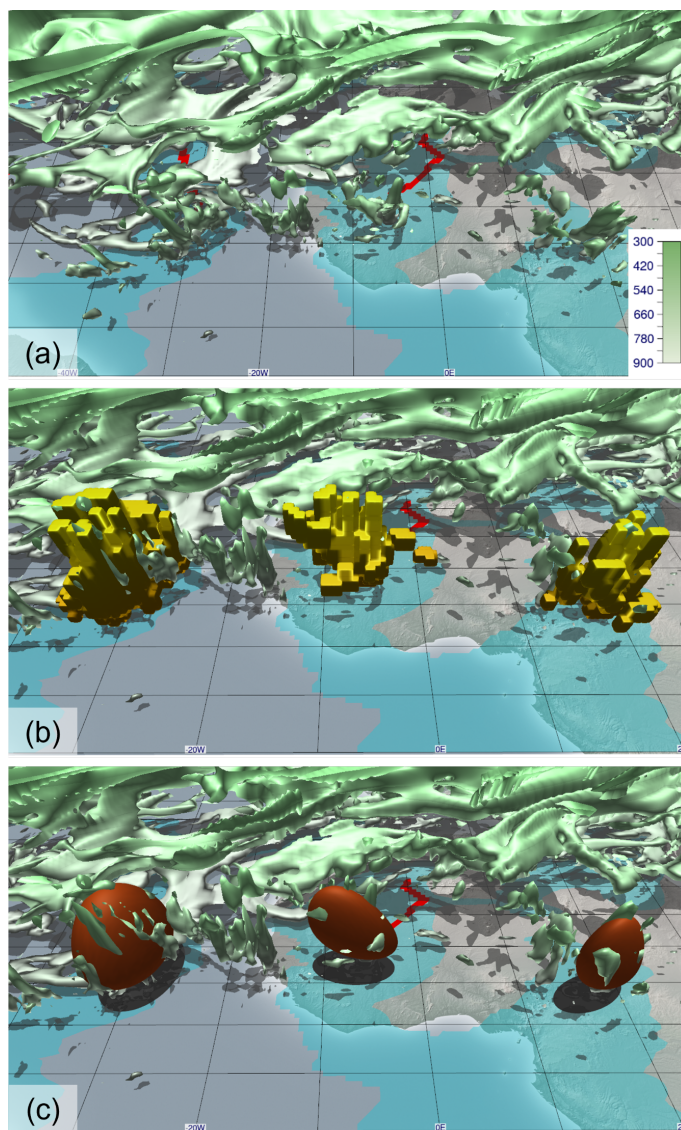
Figure 3. A 3-D visualization of the PV across the North Atlantic Ocean and West Africa at 13 September 2022, 00 UTC, created using Met.3D, is depicted. In (a), the 0.7 PVU iso-contour is displayed with shading corresponding to height, identified wave troughs in red, and the trough phase ranging from $-\pi$ to 0 is highlighted in blue. (b) showcases the identified PV objects in yellow as outlined in Sect. 2.5, while (c) illustrates the ellipsoids representing the identified features from (b).

Various approaches have been considered for computing a best-fit ellipsoid. Minimizing the squared error between the surface of the feature and the ellipsoid is computationally expensive and problematic on discrete grids (see an overview in Turner et al., 1999). An ellipsoid with the minimum volume that fully encloses the PV feature can be computed using Khachiyan's algorithm (Khachiyan, 1996), but this approach is not robust against complex features. We have determined that the most suitable method for computing ellipsoids is to calculate so-called image moments of the feature. Image moments have been widely used in image analysis and pattern recognition (e.g., Teague, 1980; Papakostas et al., 2010) as they compactly describe the spatial characteristics and geometric properties of a feature. We refer to Mukundan and Ramakrishnan (1998) for a detailed introduction of this concept. Importantly, we will exploit the second-order moments to compute the main orientation of a feature.

For a discrete setting, as for our grid, the 3-D moments M_{ijk} of order $i + j + k$ for the function PV are defined as

$$M_{ijk} = \sum_x \sum_y \sum_z x^i y^j z^k PV(x, y, z) V(x, y, z), \tag{4}$$

where PV represents the PV restricted to the identified volumetric feature (e.g., yellow structure in Fig. 3b), V the volume of the grid cell, and x, y, and z are the grid dimensions (longitude, latitude, pressure levels). Calculating the moments up to the second order provides multiple interesting characteristics of the shape. The 0th moment M_{000} represents the PV-weighted volume of the object, while the vector

$$(x_c, y_c, z_c) = \left(\frac{M_{100}}{M_{000}}, \frac{M_{010}}{M_{000}}, \frac{M_{001}}{M_{000}} \right) \tag{5}$$

represents the centroid of the feature weighted by PV. The second order moments represent the variance and covariance between each pair of dimensions. Therefore, we can construct the covariance matrix Σ of the feature as

$$\Sigma = \begin{bmatrix} \mu'_{200} & \mu'_{110} & \mu'_{101} \\ \mu'_{110} & \mu'_{020} & \mu'_{011} \\ \mu'_{101} & \mu'_{011} & \mu'_{002} \end{bmatrix}, \tag{6}$$

where $\mu'_{ijk} = \frac{M_{ijk}}{M_{000}} - x_c^i y_c^j z_c^k$ are the second order central moments. As demonstrated in Jackson (2005), the eigenvectors of the covariance matrix Σ correspond to the main axes of the feature, while the length of the main axes s_i can be computed from the eigenvalues λ_i as $s_i = 2\sqrt{\lambda_i}$. These main axes are computed for each PV feature, an example is illustrated in Fig. 3c, where the ellipsoids are the ones computed for the yellow objects in (b). Furthermore, ellipsoids are invariant under projections: Projecting ellipsoids on any 2-D plane yields ellipses (see Hartley and Zisserman, 2003), which in turn can be characterized by two main axes. We compute the projected ellipses on the three axis-aligned planes (xy, xz, and yz plane), and define these ellipses by their main axes.

2.7 Implementation Details

The feature identification and tracking and the ellipsoid computation are implemented within a framework designed for the identification and tracking of meteorological features (Fischer, 2023). This framework has been employed in previous studies
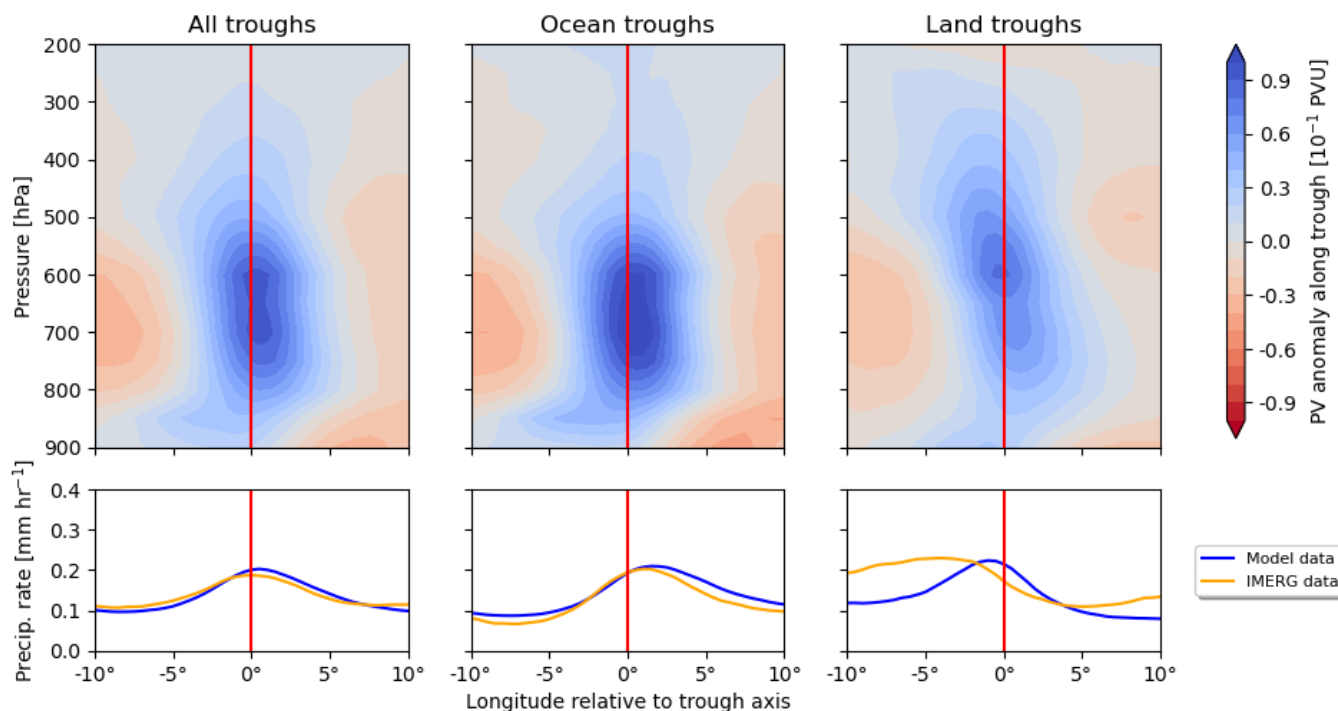
Figure 4. Composite of PV anomalies relative to the identified wave troughs along a longitude-pressure cross-section for June–October 2002–2022 based on the ERA-5 reanalysis. The red line indicates the longitude of the wave trough, with regions to the left denoting positions ahead (west) of the trough and those to the right indicating positions behind (east) of the trough. Shown are: (a) all identified wave troughs which are part of tracks, (b) focuses on the subset of troughs over the North Atlantic Ocean, and (c) focuses only on wave troughs over West Africa. In the lower panels, 6-hourly centered satellite-estimated (GPM-IMERG) and model-predicted (ERA-5 short-range forecasts) rainfall along this cross-section is visualized.

for various identification tasks (e.g., Fischer et al., 2022). It offers support for parallel execution and enables the output in JSON or Protobuf formats. Additionally, the implementation is part of the *enstools* Python package (Redl et al., 2018), which ensures robust input/output handling and incorporates efficient data processing methods. By utilizing this framework, the feature identification and ellipsoid computation processes benefit from a reliable and efficient infrastructure.

265 3 Climatology

To assess the data set generated by the identification algorithm and provide an overview of the features, a climatological analysis is conducted. As reference, Figure 4 shows a composite of the PV anomalies relative to the identified wave troughs, categorized in *Ocean* and *Land*. The categorization is based on whether the midpoint of the wave trough's bounding box is situated over tropical West Africa (Land) or the Atlantic Ocean (Ocean). For each grid point along each identified wave trough
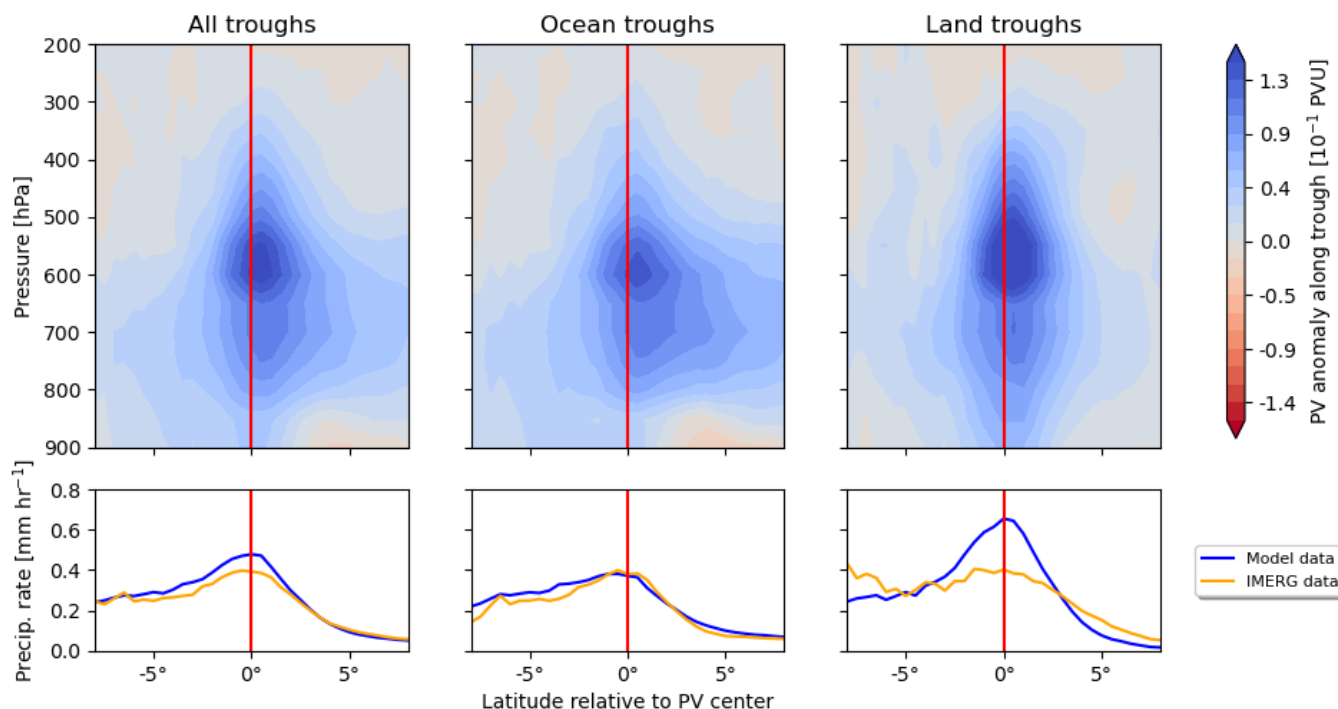
Figure 5. Similar to Fig. 4, this composite displays the latitude-pressure cross-section for the same data set, broken down in the same fashion, with the same precipitation data. The red line denotes the image moment based latitude center of the identified PV anomalies, as outlined in Sect. 2.6.

270 being part of a track, the data is split into bins based on the longitude offset ahead and behind the trough. This leads to a zonal cross section of the climatologically average AEW, looking from the south into it. Additionally, below the 3-D composites, the estimated rainfall (based on GPM-IMERG satellite retrievals), and the ERA-5 modeled rainfall is shown. The latter one is an 18-hour forecast initialized twice a day (06 UTC, 18 UTC) with hourly data available. The lead times from +6 h to +18 h are concatenated to avoid model spin up effects. Then, both the forecast's and satellite retrieval's data is centered to 6-hourly

275 around the given wave trough time to get a estimate of the rainfall rates at a given location by both data sources.

Over land, the PV column exhibits a noticeable downshear tilt (the lower tropospheric shear vector points westward due to the AEJ), whereas over the ocean, the PV column appears upright in relation to this cross-section. Moreover, over land high PV values extend higher into the troposphere than over ocean. The composite structure over land is reminiscent of the deep convection that occurs ahead of the trough (Fink and Reiner, 2003). This is corroborated by the ERA-5 model rainfall that

280 peaks slightly ahead of the trough. Over land clear differences occur, with higher estimated rainfall intensities well ahead of the trough line. As discussed in Fink and Reiner (2003), squall lines are initiated ahead of the trough, but move about twice as fast as the trough into the preceding ridge where they tend to dissipate. This is one potential explanation of the rainfall intensities increasing west of the trough in the composite. Over ocean, the PV tower is shallower and centered on the trough.

The shallower PV object over ocean is related to less deep convection over ocean due to lower CAPE values. The largest model
rainfall is found at and to the east of the trough axis. This is consistent with an AEW evolution described in Riehl (1954) and
Russell et al. (2020). The satellite-based rainfall estimations match the model rainfall in phase and amplitude quite well over
ocean.

In Figure 5, a similar composite is presented from an other viewing angle. It shows the latitude-pressure cross-section
perspective, viewing from east to west into the PV anomalies. To get a composite of PV structures independent on their current
latitude, we use here the computed center of the ellipsoid as reference latitude in the center (red line). Areas to the left indicate
locations south of the center of the PV anomaly, and areas to the right denote areas north. This view validates the PV feature
locations, aligning well with the red reference line. Over land, the PV column is upright, extending higher in the vertical,
signifying intense deep convection. Over the ocean, anomalous PV to the north of the features can be observed, particularly
between 600–700 hPa, corresponding to the level where the AEJ is strongest. Since the AEJ over the Atlantic Ocean is roughly
at 15° N (see dashed contours in Fig. 6), and the maximum of PV activity is between 10°–15° N (see shading in Fig. 6), this
lets us suggest that the PV anomaly in the composite can be traced back to PV advection taking place from tropical West Africa
to the Atlantic Ocean.

The ERA-5 modeled precipitation and rainfall estimated by satellite retrievals further match with the interpretation from the
first composite. Both data sets reveal good agreement over the ocean, while significant differences appear over land. Centered
around the trough, much less precipitation is observed. Following the argument by Fink and Reiner (2003), squall lines tend to
move faster than the trough, and therefore move out of the displayed latitude-pressure cross-section.

Figure 6 presents a climatology depicting the occurrence of wave troughs and geometrical representations. In this context,
occurrence represents the fraction of time steps within a given month where a grid point resides within the trough area intro-
duced in Sect. 2.4, indicated by the colored shading. The climatological mean zonal wind at 700 hPa, representing the AEJ,
exhibits a latitudinal movement and coincides with regions of higher wave trough occurrence. Additionally, for specific longi-
tudes, the histogram in Fig. 6f displays the amount of identified wave troughs centered at each longitude. It indicates whether
a geometric representation, as defined in Sect. 2.6, has been assigned to the respective feature. Errors during the computation
of the ellipsoid (e.g., due to an insufficient amount of data points exceeding the PV threshold) may prevent the generation of
a geometric representation for a PV feature. The plot reveals that in regions where well-developed AEWs are expected, the
majority of these waves exhibit a distinct PV signal. However, the PV signal weakens in the genesis region of northern East
Africa due to the lack of deep moist convection, and the western end of the study domain, where almost half of the waves
moving towards northern South America are accompanied with inhibition of precipitation (Giraldo-Cardenas et al., 2022).

Additionally, Fig. 7 illustrates the changes in PV feature occurrence between the months shown in Fig. 6. The mount of
PV features increase from June to July, corresponding to the West African Monsoon season's onset. Warmer and moister
atmospheric conditions favor PV anomaly formation. Then, going into August, the PV activity increases further over tropical
West Africa, aligning with peak convective activity during the monsoon season and the peak of wave activity in general
(Fink et al., 2017). Inversely to panel (a), September shows a decline in PV activity, mainly over the Atlantic Ocean, as the
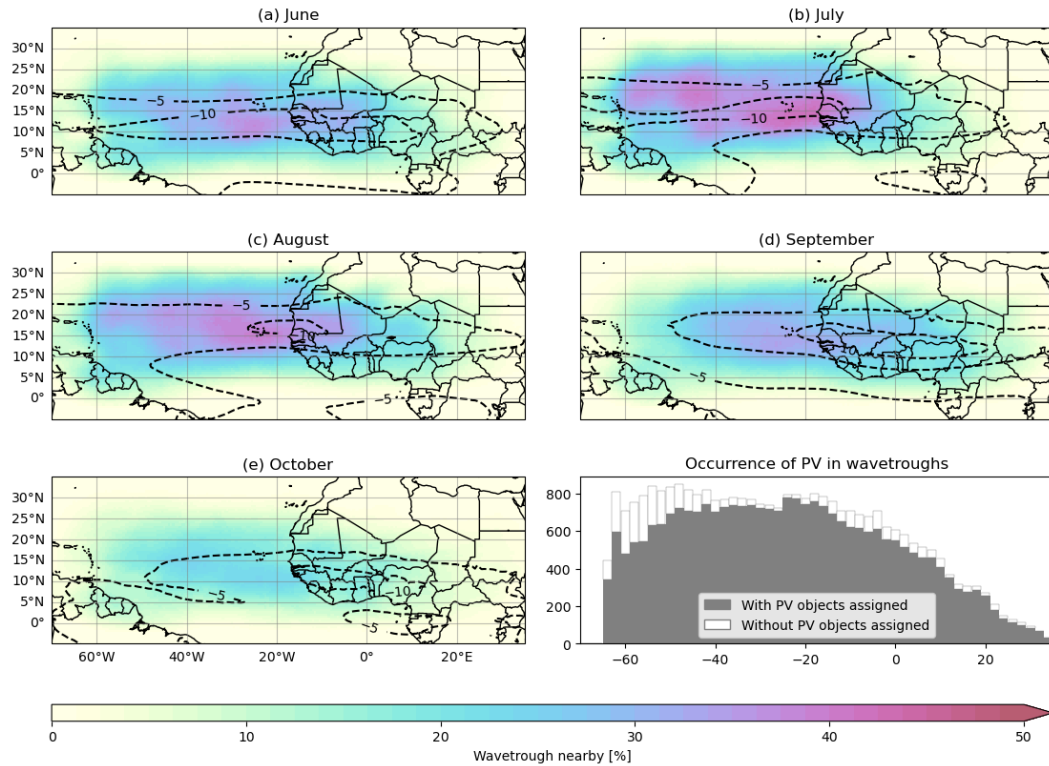
Figure 6. Occurrence percentages of trough areas for the months of (a) June to (e) October at a specific point, along with iso-lines depicting mean zonal wind at 700 hPa (-5 and -10 ms^{-1}). (f) shows the number of identified wave troughs at various longitudes based on their bounding box center, and indicates the ratio of wave troughs which have been assigned a geometric 3-D PV representation. The ERA-5 reanalysis of 2002 to 2022 has been used.

Intertropical Convergence Zone (ITCZ) shifts southward. Towards October, PV activity over West Africa retreats southward as well in tandem with the monsoon's withdrawal.

320   Figure 8 shows key characteristics of identified PV features within the study area split by longitude, more specifically their mean level and volume. As the AEWs progress from their genesis region towards 0°W, there is a noticeable upward trend in the mean level of the PV features. This upward trend in altitude suggests the evolution of the convective structure associated with the wave, evolving into deep convective structures. Subsequently, beyond 0°W, the mean level gradually decreases until approximately 40°W, indicating a descent of the diabatic heating centers in the AEWs and a shift towards lower atmospheric

325 levels. This is consistent with the composite figures and reflects less deep convection over the ocean. Changes in PV feature volume mirror the evolution of convection and diabatic processes. Peak volumes correspond to the mature phase of convective activity, aligning with the deep convection phase in these regions (Maranan et al., 2018).

    Figure 9a shows box plots depicting the orientation of PV features along the longitude-pressure plane. As described in Sect. 2.6, projecting a 3-D ellipsoid results in an ellipse, which is defined by two main axes. The more vertically oriented axis
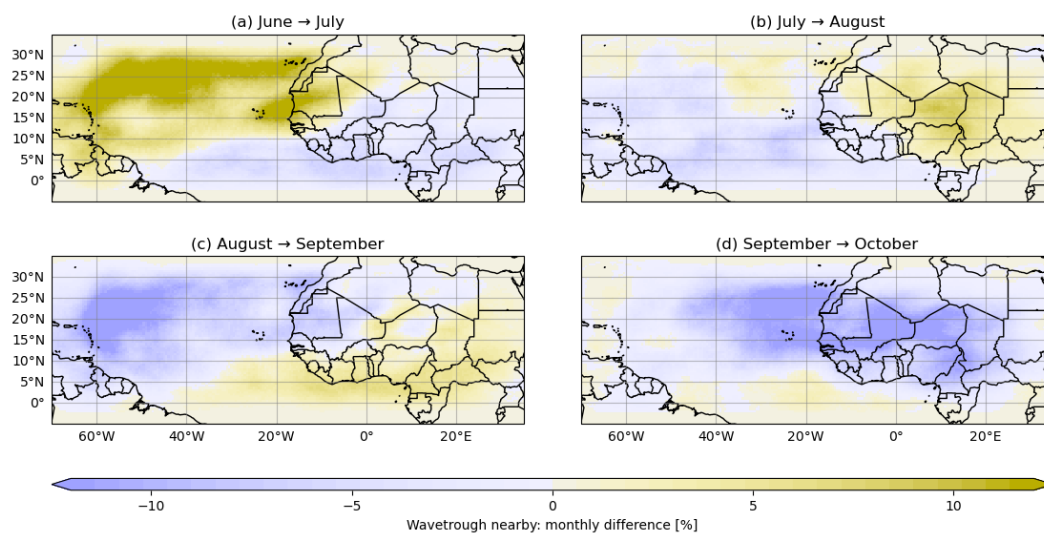
Figure 7. Differences in occurrence percentage of consecutive months in the June–October season, based on the monthly data from Fig. 6.
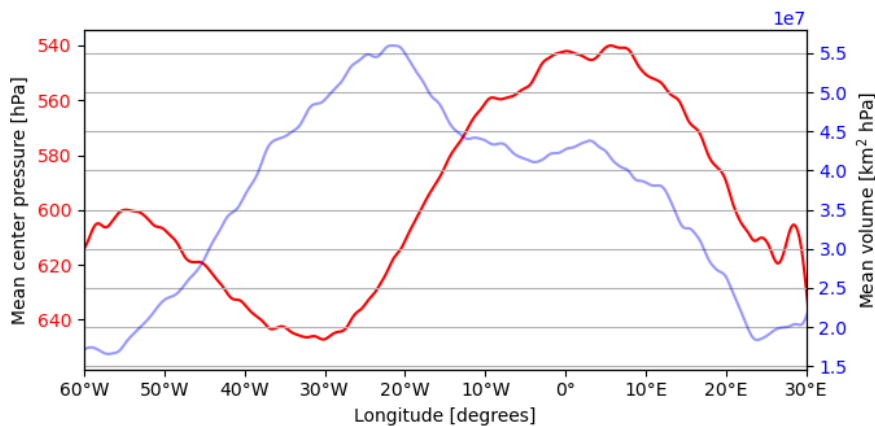
Figure 8. The mean pressure level (red) and volume (blue) for all identified PV features of the June–October 2002–2022 time span.
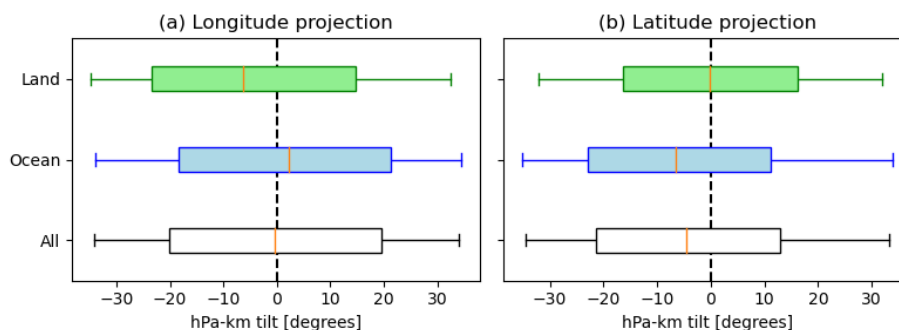
Figure 9. Orientation of projected ellipsoids on the (a) longitude-pressure plane and the (b) latitude-pressure plane. Box plots depict the orientation split by location: *Land* contain ellipsoids centered over West Africa, *Ocean* over the North Atlantic Ocean, and *All* indicate all identified features. Positive angles indicate a tilt towards higher longitude (latitude) values with height.

is used to calculate the angle of the PV feature relative to the pressure axis. The plot clearly illustrates distinct orientation patterns of PV features depending on their location. Over land, the features exhibit a downshear tilt, while over the ocean, the PV column appears upright, aligning with the composite shown in Fig. 4, validating the structure of the identified ellipsoids. Figure 9b showcases similar box plots for the latitude-pressure plane, which can be visualized by observing the PV features looking from east to west. While the longitude-pressure cross-section is visible in Fig. 4 and has been studied in the literature (e.g., Russell et al., 2020), the latitude-pressure cross-section (composite in Fig. 5) remains relatively unexplored. Here, a clear tilt pattern is evident as well, which differs between ocean and land. Over the Atlantic Ocean, the PV column tilts to the south, while it appears more upright over land, as also evident in the composite. As explained earlier, we propose that this southern tilt results from PV advection along the AEJ, inducing PV anomalies on the northern flank of the waves at lower levels and creating this asymmetry. Further research could explore the decoupling of PV sources to validate this advection process, distinguishing advection from diabatically generated PV, similar to Tomassini et al. (2017).

4   Summary & Conclusion

In this study, we have introduced a novel identification and tracking strategy for 3-D PV features within AEWs, allowing for in-depth analysis of their characteristics and statistical properties. Our algorithm builds on a robust identification and tracking of AEW troughs in 2-D at 700 hPa. Identified wave troughs and tracks for the entire ERA-5 reanalysis 1940–2022 are provided (see data availability section). Furthermore, a near real-time web-page displays wave troughs for ECMWF, GFS, and ICON forecasts. These 2-D wave troughs, combined with the computed wave phase at every point in the study domain, serve as input for the 3-D extension of our strategy, where we extract PV features associated with specific AEWs. Within the identified trough area, we collect and process PV in the column above to create cohesive structures. These PV features are further represented using best-fitting ellipsoids, enabling statistical analyses.

350   An evaluation of the feature climatology demonstrates the robustness and relevance of our approach. The occurrence, extent, and orientation of the identified PV features closely align with established expert knowledge and previous analyses within the field. Composites of PV around identified waves, both along a longitude-pressure and latitude-pressure cross-section have been computed and analyzed. These cross-sections have been computed with feature descriptors as a reference point. The results of the climatological analysis, which has been computed for the months June to October from 2002 to 2022, confirms the

355   identified feature characteristics. We conducted a comparative analysis of these PV features with estimated (GPM-IMERG) and NWP simulated (ERA-5 short-range forecast) rainfall data. Notable differences in the spatial distribution and intensity of rainfall can be observed. These disparities are primarily attributed to variations in the movement of squall lines over tropical West Africa, where satellite estimates show a much faster progression of these lines. A prominent tilt of PV features over tropical West Africa and over the North Atlantic Ocean can be observed both in the composites and in the statistical evaluation

360   of the main axes. An identified southern tilt of these features over the Atlantic suggests PV advection along the AEJ originating from the convective activity over northern Africa. Along with additional feature descriptors, like mean level and volume of the PV feature, the life-cycle of these waves can be investigated, originating as small disturbance, to deep moist convection over Africa, and towards less deep convection over the Atlantic Ocean.

   The data generated through our strategy has diverse applications. Besides the generation of feature climatologies, it can

365   be utilized as input for statistical forecasting techniques. Links between PV features and TC activity can be explored by using the features as input to statistical or mixed statistical-dynamical models (Maier-Gerber et al., 2021), as well as for forecasts of tropical rainfall over Western Africa (Vogel et al., 2021). Furthermore, our strategy enables detailed case studies and facilitates in-depth investigations of AEWs. One particular focus here could be on the relation between the 3-D PV feature evolution and the propensity of an AEW to undergo TC genesis (e.g., Dunkerton et al., 2009; Núñez Ocasio et al., 2020). In

370   all these applications, an important aspect is the sensitivity of the gross characteristics of PV features to different reanalyses or models, because the PV features can be expected to be strongly influenced by the representation of convection. In this context, differences in models with parameterized and explicit convection are considered most worthy of further study. In combination with state-of-the-art interactive 3-D visualization techniques (Rautenhaus et al., 2018), objective features also open the door for comprehensive case studies.

375   In conclusion, our study significantly contributes to the field of AEW research by providing a tool to comprehensively analyze PV features within AEWs, and thus to make the valuable PV perspective more easily applicable to AEWs. The identification and tracking strategy, along with the availability of comprehensive 3-D data, opens up new avenues for studying individual cases, understanding AEW dynamics, improving forecasts, and gaining a deeper understanding of the role of AEWs in the weather and climate of tropical West Africa and the North Atlantic Ocean.

380   *Code and data availability.*   The presented method has been implemented into *enstools-feature*, a framework for identification and tracking of meteorological features, which is available and archived at Fischer (2023). The computed data set of identified and tracked AEW troughs from the ERA-5 reanalysis is freely available and can be accessed at Fischer et al. (2023a). The data set of identified and tracked PV

features associated with these AEW troughs is freely accessible at Fischer et al. (2023b). The data sets used in this study (ERA-5 reanalysis, GPM-IMERG) are publicly available at the relevant cited sources.

385 *Author contributions.* ES, AHF, MRi and MRa supervised and administrated this study. CF designed and implemented the algorithm, performed the climatological analyses, did visualizations, and wrote the publication. All authors provided feedback on and critical review of the paper.

Competing interests. The authors declare that they have no conflict of interest.

Acknowledgements. The research leading to these results has been accomplished within the project C3 "Predictability of tropical and hybrid
390 cyclones over the North Atlantic Ocean" of the Transregional Collaborative Research Center SFB/TRR 165 "Waves to Weather" funded by the German Science Foundation (DFG). The GPM (IMERG) data were provided by the NASA/Goddard Space Flight Center, and archived at the NASA GES DISC.

References

Bain, C. L., Williams, K. D., Milton, S. F., and Heming, J. T.: Objective tracking of African Easterly Waves in Met Office models, Q. J. R. Meteorolog. Soc., 140, 47–57, https://doi.org/10.1002/qj.2110, 2014.

Belanger, J. I., Jelinek, M. T., and Curry, J. A.: A climatology of easterly waves in the tropical Western Hemisphere, Geosci. Data J., 3, 40–49, https://doi.org/10.1002/gdj3.40, 2016.

Berry, G., Thorncroft, C., and Hewson, T.: African Easterly Waves during 2004—Analysis Using Objective Techniques, Mon. Weather Rev., 135, 1251 – 1267, https://doi.org/10.1175/MWR3343.1, 2007.

Burpee, R. W.: The Origin and Structure of Easterly Waves in the Lower Troposphere of North Africa, J. Atmos. Sci., 29, 77 – 90, https://doi.org/10.1175/1520-0469(1972)029<0077:TOASOE>2.0.CO;2, 1972.

Crétat, J., Vizy, E., and Cook, K.: The relationship between African easterly waves and daily rainfall over West Africa: observations and regional climate simulations, Clim. Dyn., 44, 385–404, https://doi.org/10.1007/s00382-014-2120-x, 2015.

Diedhiou, A., Janicot, S., Viltard, A., De Felice, P., and Laurent, H.: Easterly wave regimes and associated convection over West Africa and tropical Atlantic: Results from the NCEP/NCAR and ECMWF reanalyses, Clim. Dyn., 15, 795–822, 1999.

Dunkerton, T. J., Montgomery, M. T., and Wang, Z.: Tropical cyclogenesis in a tropical wave critical layer: easterly waves, Atmos. Chem. Phys., 9, 5587–5646, https://doi.org/10.5194/acp-9-5587-2009, 2009.

Elless, T. J. and Torn, R. D.: African Easterly Wave Forecast Verification and Its Relation to Convective Errors within the ECMWF Ensemble Prediction System, Weather Forecasting, 33, 461–477, https://doi.org/10.1175/WAF-D-17-0130.1, 2018.

Elless, T. J. and Torn, R. D.: Investigating the Factors That Contribute to African Easterly Wave Intensity Forecast Uncertainty in the ECMWF Ensemble Prediction System, Mon. Weather Rev., 147, 1679–1698, https://doi.org/10.1175/MWR-D-18-0071.1, 2019.

Engel, T., Fink, A. H., Knippertz, P., Pante, G., and Bliefernicht, J.: Extreme Precipitation in the West African Cities of Dakar and Ouagadougou: Atmospheric Dynamics and Implications for Flood Risk Assessments, J. Hydrometeorol., 18, 2937 – 2957, https://doi.org/10.1175/JHM-D-16-0218.1, 2017.

Fink, A. H. and Reiner, A.: Spatiotemporal variability of the relation between African Easterly Waves and West African Squall Lines in 1998 and 1999, J. Geophys. Res.: Atmos., 108, https://doi.org/10.1029/2002JD002816, 2003.

Fink, A. H., Engel, T., Ermert, V., van der Linden, R., Schneidewind, M., Redl, R., Afiesimama, E., Thiaw, W. M., Yorke, C., Evans, M., and Janicot, S.: Mean Climate and Seasonal Cycle, chap. 1, pp. 1–39, John Wiley & Sons, Ltd, https://doi.org/10.1002/9781118391297.ch1, 2017.

Fischer, C.: enstools-feature: A framework for identification and tracking of meteorological features, https://doi.org/10.5281/zenodo.10062273, 2023.

Fischer, C., Fink, A. H., Schömer, E., van der Linden, R., Maier-Gerber, M., Rautenhaus, M., and Riemer, M.: A novel method for objective identification of 3-D potential vorticity anomalies, Geosci. Model Dev., 15, 4447–4468, https://doi.org/10.5194/gmd-15-4447-2022, 2022.

Fischer, C., Fink, A. H., Schömer, E., Rautenhaus, M., and Riemer, M.: AEWDAT - African Easterly Waves: Identified and Tracked Wave Troughs, https://doi.org/10.5281/zenodo.8403744, 2023a.

Fischer, C., Fink, A. H., Schömer, E., Rautenhaus, M., and Riemer, M.: Identified Potential Vorticity Structures associated with African Easterly Waves, https://doi.org/10.5281/zenodo.10061471, 2023b.

Giraldo-Cardenas, S., Arias, P. A., Vieira, S. C., and Zuluaga, M. D.: Easterly waves and precipitation over northern South America and the Caribbean, Int. J. Climatol., 42, 1483–1499, https://doi.org/10.1002/joc.7315, 2022.

430   Gu, G., Adler, R. F., Huffman, G. J., and Curtis, S.: African easterly waves and their association with precipitation, J. Geophys. Res.: Atmos., 109, https://doi.org/https://doi.org/10.1029/2003JD003967, 2004.

Hartley, R. and Zisserman, A.: Multiple view geometry in computer vision, Cambridge university press, 2003.

Hauser, S., Teubler, F., Riemer, M., Knippertz, P., and Grams, C. M.: Towards a holistic understanding of blocked regime dynamics through a combination of complementary diagnostic perspectives, Weather Clim. Dyn., 4, 399–425, https://doi.org/10.5194/wcd-4-399-2023, 2023.

435   Hengstebeck, T., Heizenreder, D., Joe, P., and Lang, P.: The mesocyclone detection algorithm of DWD, in: 6th European Conference on Severe Storms, ECSS, pp. 3–7, 2011.

Hersbach, H., Bell, B., Berrisford, P., Hirahara, S., Horányi, A., Muñoz-Sabater, J., Nicolas, J., Peubey, C., Radu, R., Schepers, D., Simmons, A., Soci, C., Abdalla, S., Abellan, X., Balsamo, G., Bechtold, P., Biavati, G., Bidlot, J., Bonavita, M., De Chiara, G., Dahlgren, P., Dee, D., Diamantakis, M., Dragani, R., Flemming, J., Forbes, R., Fuentes, M., Geer, A., Haimberger, L., Healy, S., Hogan, R. J., Hólm, E.,

440   Janisková, M., Keeley, S., Laloyaux, P., Lopez, P., Lupu, C., Radnoti, G., de Rosnay, P., Rozum, I., Vamborg, F., Villaume, S., and Thépaut, J.-N.: The ERA5 global reanalysis, Q. J. Roy. Meteor. Soc., 146, 1999–2049, https://doi.org/10.1002/qj.3803, 2020.

Hoskins, B. J., McIntyre, M. E., and Robertson, A. W.: On the use and significance of isentropic potential vorticity maps, Q. J. R. Meteorolog. Soc., 111, 877–946, https://doi.org/10.1002/qj.49711147002, 1985.

Huffman, G. J., Bolvin, D. T., Nelkin, E. J., and Tan, J.: Integrated Multi-satellitE Retrievals for GPM (IMERG) technical documentation,

445   NASA/GSFC Code, 612, 2019, 2015.

Jackson, J. E.: A user's guide to principal components, John Wiley & Sons, 2005.

Josipovic, L., Werner, M., Feger, R., Wapler, K., Schultze, M., and Blahak, U.: Object-based Nowcasting at DWD using KONRAD3D, HYMEC, and Lightning Data, Tech. Rep. 19, Copernicus Meetings, https://doi.org/10.5194/ems2022-659, 2022.

Khachiyan, L. G.: Rounding of Polytopes in the Real Number Model of Computation, Math. Oper. Res., 21, 307–320,

450   https://doi.org/10.1287/moor.21.2.307, 1996.

Limbach, S., Schömer, E., and Wernli, H.: Detection, tracking and event localization of jet stream features in 4-D atmospheric data, Geosci. Model Dev., 5, 457–470, https://doi.org/10.5194/gmd-5-457-2012, 2012.

Maier-Gerber, M., Fink, A. H., Riemer, M., Schoemer, E., Fischer, C., and Schulz, B.: Statistical–Dynamical Forecasting of Subseasonal North Atlantic Tropical Cyclone Occurrence, Weather Forecasting, 36, 2127 – 2142, https://doi.org/10.1175/WAF-D-21-0020.1, 2021.

455   Maranan, M., Fink, A. H., and Knippertz, P.: Rainfall types over southern West Africa: Objective identification, climatology and synoptic environment, Q. J. R. Meteorolog. Soc., 144, 1628–1648, https://doi.org/10.1002/qj.3345, 2018.

McIntyre, M. E. and Palmer, T.: Breaking planetary waves in the stratosphere, Nature, 305, 593–600, https://doi.org/10.1038/305593a0, 1983.

Mukundan, R. and Ramakrishnan, K. R.: Moment Functions in Image Analysis — Theory and Applications, World scientific,

460   https://doi.org/10.1142/3838, 1998.

Müller, A., Niedrich, B., and Névir, P.: Three-dimensional potential vorticity structures for extreme precipitation events on the convective scale, Tellus A: Dyn. Meteorol. Oceanogr., 72, 1–20, https://doi.org/10.1080/16000870.2020.1811535, 2020.

Najman, L. and Talbot, H.: Mathematical morphology: from theory to applications, John Wiley & Sons, 2013.

Núñez Ocasio, K. M., Evans, J. L., and Young, G. S.: A Wave-Relative Framework Analysis of AEW–MCS Interactions Leading to Tropical

465   Cyclogenesis, Mon. Weather Rev., 148, 4657–4671, https://doi.org/10.1175/MWR-D-20-0152.1, 2020.

Papakostas, G., Koulouriotis, D., and Karakasis, E.: Computation strategies of orthogonal image moments: A comparative study, Appl. Math. Comput., 216, 1–17, https://doi.org/10.1016/j.amc.2010.01.051, 2010.

Purves, S.: Phase and the Hilbert transform, The Leading Edge, 33, 1164–1166, https://doi.org/10.1190/tle33101164.1, 2014.

Rasp, S. and Lerch, S.: Neural Networks for Postprocessing Ensemble Weather Forecasts, Mon. Weather Rev., 146, 3885 – 3900, https://doi.org/https://doi.org/10.1175/MWR-D-18-0187.1, 2018.

Rautenhaus, M., Grams, C. M., Schäfler, A., and Westermann, R.: Three-dimensional visualization of ensemble weather forecasts – Part 2: Forecasting warm conveyor belt situations for aircraft-based field campaigns, Geosci. Model Dev., 8, 2355–2377, https://doi.org/10.5194/gmd-8-2355-2015, 2015a.

Rautenhaus, M., Kern, M., Schäfler, A., and Westermann, R.: Three-dimensional visualization of ensemble weather forecasts – Part 1: The visualization tool Met.3D (version 1.0), Geosci. Model Dev., 8, 2329–2353, https://doi.org/10.5194/gmd-8-2329-2015, 2015b.

Rautenhaus, M., Böttinger, M., Siemen, S., Hoffman, R., Kirby, R. M., Mirzargar, M., Röber, N., and Westermann, R.: Visualization in meteorology—a survey of techniques and tools for data analysis tasks, IEEE T. Vis. Comput. Gr., 24, 3268–3296, https://doi.org/10.1109/TVCG.2017.2779501, 2018.

Redl, R., Keil, C., Craig, G., Lerch, S., and Eichhorn, J.: Towards a Framework for Parallelized Post-Processing and Evaluation of Ensemble Forecasts, in: EGU General Assembly Conference Abstracts, EGU General Assembly Conference Abstracts, p. 12322, 2018.

Reed, R., Klinker, E., and Hollingsworth, A.: The structure and characteristics of African easterly wave disturbances as determined from the ECMWF operational analysis/forecast system, Meteorol. Atmos. Phys., 38, 22–33, 1988.

Reed, R. J., Norquist, D. C., and Recker, E. E.: The Structure and Properties of African Wave Disturbances as Observed During Phase III of GATE, Mon. Weather Rev., 105, 317–333, https://doi.org/10.1175/1520-0493(1977)1052.0.CO;2, 1977.

Riehl, H.: Tropical Meteorology, chap. 9, pp. 210–234, McGraw-Hill Book Co., 1954.

Russell, J. O., Aiyyer, A., White, J. D., and Hannah, W.: Revisiting the connection between African Easterly Waves and Atlantic tropical cyclogenesis, Geophys. Res. Lett., 44, 587–595, https://doi.org/10.1002/2016GL071236, 2017.

Russell, J. O. H., Aiyyer, A., and Dylan White, J.: African Easterly Wave Dynamics in Convection-Permitting Simulations: Rotational Stratiform Instability as a Conceptual Model, J. Adv. Model. Earth Syst., 12, e2019MS001 706, https://doi.org/10.1029/2019MS001706, 2020.

Shapiro, L. J.: The Vorticity Budget of a Composite African Tropical Wave Disturbance, Mon. Weather Rev., 106, 806 – 817, https://doi.org/10.1175/1520-0493(1978)106<0806:TVBOAC>2.0.CO;2, 1978.

Smith, W. L. and Woolf, H. M.: The Use of Eigenvectors of Statistical Covariance Matrices for Interpreting Satellite Sounding Radiometer Observations, J. Atmos. Sci., 33, 1127–1140, https://doi.org/10.1175/1520-0469(1976)0332.0.CO;2, 1976.

Teague, M. R.: Image analysis via the general theory of moments, J. Opt. Soc. Am., 70, 920–930, https://doi.org/10.1364/JOSA.70.000920, 1980.

Teubler, F. and Riemer, M.: Potential-vorticity dynamics of troughs and ridges within Rossby wave packets during a 40-year reanalysis period, Weather Clim. Dyn., 2, 535–559, https://doi.org/10.5194/wcd-2-535-2021, 2021.

Thorncroft, C. and Hodges, K.: African Easterly Wave Variability and Its Relationship to Atlantic Tropical Cyclone Activity, J. Clim., 14, 1166 – 1179, https://doi.org/10.1175/1520-0442(2001)014<1166:AEWVAI>2.0.CO;2, 2001.

Thorncroft, C. D., Hoskins, B. J., and McIntyre, M. E.: Two paradigms of baroclinic-wave life-cycle behaviour, Q. J. Roy. Meteor. Soc., 119, 17–55, https://doi.org/10.1002/qj.49711950903, 1993.

Thorncroft, C. D., Hall, N. M. J., and Kiladis, G. N.: Three-Dimensional Structure and Dynamics of African Easterly Waves. Part III: Genesis, J. Atmos. Sci., 65, 3596 – 3607, https://doi.org/10.1175/2008JAS2575.1, 2008.

505 Tomassini, L., Parker, D. J., Stirling, A., Bain, C., Senior, C., and Milton, S.: The interaction between moist diabatic processes and the atmospheric circulation in African Easterly Wave propagation, Q. J. R. Meteorolog. Soc., 143, 3207–3227, https://doi.org/10.1002/qj.3173, 2017.

Turner, D., Anderson, I., and Mason, J.: An algorithm for fitting and ellipsoid to data, Technical Report, Tech. Rep. RR9803, School of Computing and Mathematics, University of Huddersfield, 1999.

510 Vogel, P., Knippertz, P., Gneiting, T., Fink, A. H., Klar, M., and Schlueter, A.: Statistical Forecasts for the Occurrence of Precipitation Outperform Global Models over Northern Tropical Africa, Geophys. Res. Lett., 48, e2020GL091 022, https://doi.org/10.1029/2020GL091022, 2021.

Weijenborg, C., Chagnon, J., Friederichs, P., Gray, S., and Hense, A.: Coherent evolution of potential vorticity anomalies associated with deep moist convection, Q. J. Roy. Meteor. Soc., 143, 1254–1267, https://doi.org/10.1002/qj.3000, 2017.

515 Zimin, A. V., Szunyogh, I., Patil, D. J., Hunt, B. R., and Ott, E.: Extracting Envelopes of Rossby Wave Packets, Mon. Weather Rev., 131, 1011 – 1017, https://doi.org/10.1175/1520-0493(2003)131<1011:EEORWP>2.0.CO;2, 2003.